Transonic Blade-Vortex Interactions Noise: A Parametric Study

Lyrintzis, A. S.* and Xue, Y.**

Aerospace Engineering & Mechanics

University of Minnesota, Minneapolis, MN 55455

Abstract

Transonic Blade-Vortex Interactions (BVI) are simulated numerically and the noise mechanisms are investigated. The two-dimensional high frequency transonic small disturbance equation is solved numerically (VTRAN2 code). An ADI scheme with monotone switches is used; viscous effects are included on the boundary and the vortex is simulated by the cloud-in-cell method. The Kirchhoff method is used for the extension of the numerical two-dimensional near-field aerodynamic results to the linear acoustic three-dimensional far-field. The viscous effect (shock/boundary layer interaction) on BVI is investigated. The different types of shock motion are identified and compared. Two important disturbances with different directivity exist in the pressure signal and are believed to be related to the fluctuating lift and drag forces. Noise directivity for different cases is shown. The maximum radiation occurs at an angle between 60° and 90° below the horizontal for an airfoil-fixed coordinate system and depends on the details of the airfoil shape. Different airfoil shapes are studied and classified according to the BVI noise produced.

----

* Assistant Professor.
** Graduate student.

In references [16-24] the two-dimensional transonic BVI problem is also solved using the small disturbance theory and the more complex Euler and thin-layer Navier Stokes equations. Also Baeder et al. [22, 23] and Liu et al. [24] presented some near and mid field results. A direct comparison of the results obtained from the different methods (from small disturbance to Navier Stokes equations) shows that the results are very similar [7]. In fact the results tend to coincide the further away we move from the airfoil surface. At great distances from the airfoil though, the waves become very difficult to follow because of numerical diffusion and dispersion errors.

The Kirchhoff method was introduced [14, 25-29] to extend the numerically calculated nonlinear aerodynamic results to the linear acoustic far-field. This method uses a Green's function for the linearized governing equation to derive a representation for the solution in terms of its values and derivatives on a closed surface S in space, which is assumed to include all the nonlinear flow effects and noise sources. The potential and its derivatives can be numerically calculated from a nonlinear aerodynamic code (e. g. VTRAN2). The Kirchhoff method has the advantage of including the full diffraction effects and eliminates the erroneous propagation of the reactive near-field.

In this paper we examine the noise due to BVI. The viscous effect (shock/boundary layer interaction) on BVI noise is studied. The resulting noise because of the different types of shock-wave motion types A, B and C in the near- and the far-field is investigated and the different resulting disturbances are analyzed. The noise mechanisms are explained physically and the relation between the noise signal and oscillating lift and drag forces is shown. The complicated directivity patterns of BVI noise are also studied. Different airfoil shapes are studied and classified according to the produced BVI noise.

The Numerical Method (VTRAN2)

VTRAN2 is a code [13, 14] developed for analyzing the interactions of convected regions of vorticity with airfoils using transonic small disturbance theory. It is based on the ADI implicit scheme of the LTRAN2 code [8] with the inclusion of the high frequency term as described in reference [9] and the addition of regions of convected vorticity using the cloud-in-cell and multiple branch-cut approach. The code was modified to include viscosity [8] and monotone switches [10].

3

The equation for the unsteady transonic small-disturbance potential ϕ is:

$$A\phi_{tt} + 2B\phi_{xt} = C\phi_{xx} + \phi_{yy} \tag{1}$$

where

$$A = \frac{k^2 M^2}{\delta^{2/3}}, \quad B = \frac{kM^2}{\delta^{2/3}}, \quad C = \frac{1-M^2}{\delta^{2/3}} - (\gamma+1)M^m \phi_x,$$

ϕ is the disturbance-velocity potential, M is the free-stream Mach number, δ is the airfoil thickness ratio and k is the reduced frequency $\omega c/U_0$ where ω is the characteristic frequency of the unsteady motion, c is the airfoil chordlength and U_0 is the free stream velocity. The quantities x, y, t, ϕ in equation 1 have been scaled by c, $c/\delta^{1/3}$, ω^{-1}, and $c\delta^{2/3} U_0$, respectively. The exponent m in the nonlinear term is chosen as m = 2, which is suitable for stronger shocks as it locates the shocks more accurately [30].

For BVI the characteristic frequency of the motion depends on the lateral distance between the airfoil and the vortex path. For large miss distances y_v the characteristic frequency ω is U_0/y_v and thus $k=c/y_v \ll 1$. Therefore, the k^2 term in A implies that the first term (i. e. high frequency term) in equation (1) can be dropped giving the low frequency small disturbance theory, which was used in the LTRAN2 code. However, for BVI cases of interest $y_v \approx c$, and thus $k \approx 1$ and the full small disturbance equation (1) (including the high frequency term) is needed. Since time t is nondimensionalized, the choice of k for the case of BVI is irrelevant and was taken as k=1 ($\omega = U_0/c$), meaning that one time unit corresponds to a free stream convection of one chord.

The boundary conditions are:

1. Upstream outer boundary condition:

$$\phi_x = \phi_y = 0 \quad \text{as } x \to -\infty \tag{2}$$

2. Lateral outer boundary condition:

$$\phi_x = \phi_y = 0 \quad \text{as } y \to \pm\infty \tag{3}$$

3. Downstream outer boundary condition:

$$\phi_x + k\phi_t = 0 \quad \text{as } x \to +\infty \tag{4}$$

4. Airfoil surface boundary condition (applied at y=0):

$$\phi_y = \frac{\partial Y\pm}{\partial x} + k\frac{\partial Y\pm}{\partial t} \quad \text{as } 0 < x < c \tag{5}$$

where $Y\pm$ defines the airfoil surface.

For the viscosity calculations the viscous ramp method (wedge) is used. The viscous ramp model simulates the shock/boundary layer interaction by placing a wedge-nosed ramp at the base of the shock to obtain the reduced shock pressure rise. The surface geometry must be augmented by the ramp model by adding an extra viscous term in the boundary condition of equation (5). Details of the calculation of that viscous term can be found in reference [31]. The ramp model was derived for steady-state computations. However, it can be incorporated into unsteady computations in a quasi-steady fashion. Thus, the model is valid for low frequencies, and its use in high frequency problems such as BVI can only give some qualitative information about the effect of viscosity with almost no additional CPU time. The more complicated and CPU time-consuming lag-entrainment method which was also incorporated in our code was not used, because it was not superior to the wedge model for unsteady cases [31].

The classical Kutta condition is satisfied by this small disturbance formulation. We are interested in cases for which the reduced frequency range is less than 4, which is the limit for the application of the Kutta condition [32].

The pressure coefficient C_p in the unsteady small-disturbance theory is:

$$C_p = -2\delta^{2/3}(\phi_x + k\phi_t) \tag{6}$$

In addition, the wake condition

$$\Gamma_x + k\Gamma_t = 0 \tag{7}$$

implies that a branch cut exists between the trailing edge and the downstream outer boundary, across which the potential jump is, $\Delta\phi = \Gamma$, where Γ is the circulation.

A finite vortex core is used (cloud-in-cell method) for reasons of computational stability. The core has a finite square shape limited by gridlines and the vorticity is bilinearly distributed inside. Thus, several branch cuts (in the x-direction) are introduced. The vortex can have a free path (convected by the flow) or a prescribed path (miss distance y_v = constant, vortex velocity=U_o). Details of the theoretical formulation were given by Chang [33] and Lyrintzis [14].

An alternating direction implicit (ADI) method is used for the solution of the equation, where the high frequency term is added in the y-sweep. An approximate factorization technique with monotone

switches [11] is used for the steady calculation, which provides a start-up solution. Special care is taken for the conservative differentiation along the uneven mesh.

A (213x199) mesh is used for the calculations. The computational mesh points are clustered more densely near and in front of the airfoil and then are stretched exponentially from the near airfoil region to about 200 chords from the airfoil in x and 400 in y-direction. More mesh points are added in the y-direction for the more accurate evaluation of the normal derivatives on the Kirchhoff surface. The VTRAN2 code was shown to agree well with other, more complex approaches including Euler and thin-layer Navier-Stokes computations [7]. The code has a high vectorization level and the CPU time for each two-dimensional case on a Cray-2 computer is about 4 minutes for 800 time-marching steps.

Kirchhoff's Method for the Far-Field

The Kirchhoff equation for a moving surface was originally derived by Morgans [34]. A Green's function approach will be used to derive the Kirchhoff formula in a coordinate system fixed to the airfoil which moves with velocity U_0. The Green's function approach was introduced by Morino [35, 36]. Farassat and Myers [37] rederived the Kirchhoff equation for an arbitrarily moving piecewise smooth deformable surface using generalized derivatives. A very brief discussion of the Kirchhoff formulation is given in the following paragraphs; for more details the reader is referred to the above references, and also references [14, 26].

A Green's function for the linearized governing equation is used to derive a representation for the solution in terms of its values and derivatives on a closed surface S in space, which is assumed to include all the nonlinear flow effects and noise sources. A full three-dimensional formulation is used, because the Green's function is simpler in this case, and because the method can be easily extended to include spanwise variations to model three-dimensional BVI. The pressure distribution outside a rigid fixed surface is

$$p(x_0,y_0,z_0) = -\frac{1}{4\pi} \int_S \left[\frac{1}{r_0} \frac{\partial p}{\partial n_0} + \frac{1}{c_0 r_0 \beta^2} \frac{\partial p}{\partial t} \left(\frac{\partial r_0}{\partial n_0} - M \frac{\partial x'_0}{\partial n_0} \right) + \frac{p}{r_0^2} \frac{\partial r_0}{\partial n_0} \right]_\tau dS'_0 \qquad (8)$$

where
$$r_0 = \{(x-x')^2 + \beta^2[(y-y')^2 + (z-z')^2]\}^{1/2}$$

$$\tau = \frac{[r_0 - M(x-x')]}{c_0\beta^2}$$

$$\beta = (1-M^2)^{1/2}$$

where " ' " denotes a point on the Kirchhoff surface, subscript o denotes the transformed values using the well known Prandtl-Glauert transformation:

$$x_0 = x, \quad y_0 = \beta y, \quad z_0 = \beta z$$

n is the outward vector normal to the surface S, and subscript τ implies the evaluation at the retarded time $t_1 = t-\tau$.

Thus, the values of the potential and its normal derivatives on an arbitrary surface around the spanwise extent of an arbitrary flow are enough to give the far-field radiation at any arbitrary external point. In our work we use a rectangular box coinciding with mesh points in order to simplify the computation. The control volume is shown in figure 3. The potential and its derivatives can be numerically calculated from an aerodynamic near-field code.

Since Kirchhoff's method assumes that linear equations hold outside this control surface S, it must be chosen large enough to include the region of nonlinear behavior. However, due to increasing mesh spacing the accuracy of the numerical solution is limited to the region immediately surrounding the moving blade. As a result S cannot be so large as to lose accuracy in the numerical solution for the mid-field. Therefore, a judicious choice of S is required for the effectiveness of the Kirchhoff method. A rectangular box-shaped surface (fig. 3) is used for the calculations. The VTRAN2 code is used to calculate the solutions on the surface S. The y-limits of S for our calculations are varied over a range from $y_s = 0.25$ to 4.00 chords distance from the airfoil. Higher Mach numbers yield higher optimum values for y_s because of stronger nonlinearities in the larger lateral extent of the flow region. The x-limits for S were also varied between 0.15 and 0.50 chords and, similarly, values of 0.25 chords upstream and downstream of the leading and trailing edges respectively, are chosen.

Strip theory approximation is used; that is, the two-dimensional VTRAN2 solution is applied on different segments of the blade in a stripwise manner. Blade segments ranging from two to sixteen in aspect ratio are used. Usually mesh limitations keep the Kirchhoff surface close enough to the blade where the two-dimensional strip theory solution is still valid. By making calculations with or without

7

the inclusion of the tip surfaces we found [27] that they have only a small effect; thus they were neglected for most of the calculations.

Types of Unsteady Shock Motion

Tijdeman [38] showed experimentally, using an oscillating flap, that varying airfoil surface boundary conditions can give three different types of unsteady shock motion (figure 4):

Type A shock motion, where the shock at the rear of the supersonic region merely moves back and forth with concurrent changes in strength.

Type B shock motion, where the shock moves similarly to type A, but disappears temporarily during the unsteady motion.

Type C shock motion, where the supersonic region disappears, but a shock wave leaves the airfoil and propagates forward to the far-field.

The above three types of unsteady shock motions affect heavily the characteristics (e. g. lift, drag) of all unsteady transonic flows. The type of shock motion that occurs in a given situation depends on the flow characteristics (e. g. free stream Mach number, airfoil shape, amplitude and frequency of the unsteady motion). These types of shock motion can even be observed in steady airfoils with severe flow separation downstream of the shock waves. Their existence in BVI has been verified by different experiments and calculations (e. g. Tangler's experiments [39]).

Results and Discussion

Some mid-field calculations for BVI are performed using VTRAN2 with a refined mesh to follow the waves of interest. Then the Kirchhoff method is used to look at the noise at the far-field. The calculations are made in an airfoil-fixed reference frame. A more detailed discussion of the coordinate systems used for BVI calculations is given in reference [25].

The three different types of the unsteady shock motion are studied. We use a NACA 64A006 airfoil, the vortex strength was $C_{lv}=0.4$ (C_{lv} is a nondimensional measure of the vortex strength: $C_{lv}=2\Gamma/cU_0$) and the vortex miss-distance $y_0=-0.5$ chords, for a fixed vortex path. The initial vortex position is -9.51 chords and the free stream velocity is one (arbitrary units) so the vortex passes below the airfoil leading edge at time $T = 9.51$. The Mach numbers of 0.875, 0.854, and 0.822

8

correspond to shock wave motions of types A, B, and C, respectively, as also shown in reference [7]. For the Kirchhoff surface (fig. 3) we used a span of 8 chords, $x_s = 0.25$ chords and $y_s = 3.5$, 2.5 and 1.9 chords for the three types A, B and C, respectively. Note that a larger y_s is required for higher Mach numbers, because the y-extent of the nonlinear region of the flow increases, as expected from the scaling laws of transonic flow.

Figure 5 shows the effect of the grid on the lift coefficient $C_l(T)$. A standard mesh (213x119) is compared to a finer in the y-direction mesh (213x199). The results show that the fine mesh produces a smoother solution. Smoother solutions are also produced for the pressure coefficient at different points, especially in the far-field using the Kirchhoff method. Finer meshes were also tried, but the results were not substantially changed. Thus, the fine mesh (213x199) will be used in the subsequent calculations.

Figures 6, 7 and 8 show the effect of viscosity in the calculations. The pressure coefficient $C_p(T)$ at point P (-0.3000, -0.17478), the lift coefficient $C_l(T)$ and the drag coefficient $C_d(T)$ are plotted for a type A shock motion, for viscous and nonviscous calculations. We can see only a slight influence of the effect of viscosity. Since viscosity is added as an extra boundary condition to model shock/boundary layer interaction, we expect the influence to be stronger with the increase of the strength of the shock. Thus, the effect of viscosity is lower for the types B and C (not shown) and zero for subcritical cases. The following results will include the effect of the viscosity.

Figures 9 and 10 show the $C_p(T)$ signal of the three types of unsteady shock motion in the mid-field (point P) from VTRAN2 and in the far-field (point O, r=20 chords, $\theta=30^o$) from Kirchhoff. The signal consists of three disturbances (I, II, III) as also shown in references [25, 26]. The primary disturbance I is the main BVI noise and it originates at the airfoil when the vortex passes below the leading edge. It is believed to be related to the fluctuating lift coefficient C_l. The secondary disturbance II corresponds to the unsteady shock motion and depends on the motion of the whole supersonic region induced by the vortex passage. It originates at the airfoil at a later time, and depends heavily on the type of shock motion. It is believed to be somehow related to the fluctuating drag coefficient C_d. The existence of the second disturbance was observed computationally by George and Chang [7] and was also verified experimentally by Caradonna et al. [40] and Shenoy

9

[41], and computationally by George and Lyrintzis [25, 26], Owen and Shenoy [20] and Liu *et al.* [24]. Disturbance II disappears if we run subcritical cases. The directivity of the two disturbances is very different as will be shown later. Disturbance III is considered to be an standing disturbance due to the vortex passage and it is not a propagating wave. Thus this disturbance disappears as we move from the mid-field (fig.9) to the far-field (fig. 10).

From figures 9 and 10 we can see that disturbance I increases slightly with increasing Mach number. We should also bear in mind that the definition of C_p includes division by M^2, so the effect of the Mach number is stronger than it appears in the above figures. Disturbance II exists also for type A and B shock motions, because it is caused by the movement of the whole supersonic pocket, and seems to be magnified as we move into the far-field. It also appears to be decreasing as we move from type C to type A. However, if we measure it from peak to peak it still increases, but at a lower rate from disturbance I. Disturbance III is almost same for the three cases, which seems reasonable since the same vortex strength is used.

Figure 11 shows the lift coefficient C_l (T) for types A, B and C. We can see that their shapes relate well to the first disturbances shown in previous figures. Specifically the total C_l change for the type A shock motion is much higher than that for type C. Thus, we can deduce that disturbance I is most probably related to C_l.

The drag coefficient C_d will be discussed next. It is well known that in subcritical inviscid flow C_d is zero. It should be noted though, that C_d is not zero for subcritical inviscid flow due to numerical errors of the code, but it is much lower than the C_d in supercritical cases. Thus, the calculated C_d values are only indicative and will be used only for comparison of the three unsteady types of shock motion. When the flow becomes supercritical, then C_d is not theoretically zero, even for inviscid flow, because of the formation of supersonic pockets. C_d can be easily calculated if the pressure distribution is known. Figure 12 shows C_d (T) for types A, B and C . The C_d signal seems to catch some part of the second disturbance whereas C_l does not. This was also detected by Liu *et al.* [24] for some BVI cases using a thin layer Navier Stokes code, but is easier to see in the case of an oscillating flap [15], because there the periodicity of the motion is well-defined. Thus, we

can conclude that the second disturbance is most probably related to the fluctuating C_d caused mainly by the movement of the supersonic pocket.

In order to verify the above arguments we compared results from airfoils with the same thickness distribution (i. e. same family) but different camber, in conditions producing the same lift (i. e. different angle of attack). Figure 13 compares the $C_p(T)$ BVI signals for the far-field (point O) for a NACA 1406 airfoil at an angle of attack $\alpha=0^o$, for a NACA (0.5)406 at $\alpha=0.536^o$ and for a NACA 0006 at $\alpha=1.051^o$. These conditions, with a standing vortex upstream, produce initial $C_l=0.229$. In fact, the whole unsteady lift $C_l(T)$ for these cases is almost the same, whereas the unsteady drag $C_d(T)$ is not. All the airfoils have a type A shock motion for these conditions. We can see from figure 13 that disturbance I remains unchanged, whereas disturbance II does change, becoming higher as the camber increases. This agrees with our earlier discussion of lift and drag forces.

We also looked at the effect of the point of maximum camber. In figure 14 we compared the $C_p(T)$ BVI signals for the far-field (point O) for NACA airfoils with different point of maximum camber: 1306 and 1406, for angles of attack that produce the same lift: $\alpha=0.055^o$ and 0°, respectively. We can see from figure 14 that disturbance I remains unchanged, whereas disturbance II becomes larger as the point of maximum camber moves downstream. Thus, the 1406 airfoil has the larger disturbance II.

From figures 13 and 14 we can conclude that disturbance I is related to the lift and disturbance II is related to the details of the airfoil shape, which produce a different supersonic pocket and thus a different drag. Symmetric airfoils and airfoils with the point of maximum camber further upstream give a lower value of disturbance II, for the same lift.

A parametric study showed [26] that the vortex strength has a strong effect on the noise signal, whereas the vortex miss distance has only a weak effect. The maximum airfoil thickness and the details of airfoil shape were also found to be important. A more detailed parametric study is currently [29] being carried out.

The directivity of the noise signal in the far-field is very complicated, as has been shown by experimental studies. Most of these experiments are also three-dimensional, which makes them very

11

difficult to compare. For example, in reference [42] it was shown for a model helicopter rotor that the maximum signal can have a different direction if the advance ratio μ is varied.

Directivity is studied in a vortex-fixed coordinate system keeping the distance from the vortex r_v constant ($r_v = 50$ chords). The relationship between θ and θ_v is shown in figure 15. The Cp(t) signal for different directions is plotted in figures 16, 17, 18 for types A, B and C shock motion, respectively (note that span = 4 chords for this case). By analyzing the plots, we can see that disturbance I is getting weaker as the direction angle θ increases from 0° to 90° (forward directivity). Disturbance II is getting stronger as the direction angle θ increases from 0° to 90° (downward directivity). The two disturbances also move closer as the angle θ is increased, and finally almost merge at $\theta =120^o$. This implies a different origin. If the origin of disturbance I is at the airfoil leading edge, the origin of disturbance II is probably somewhere downstream since this disturbance is related to the movement of the supersonic pocket.

It should be noted that for an oscillating flap [15] the opposite directivity was observed: downward for disturbance I and forward for disturbance II. Thus, it was concluded that disturbance I is due to the dipole produced from oscillating lift and disturbance II is produced from oscillating drag. If we run a subcritical case then disturbance II disappears, as expected, and the directivity of disturbance I is downward (disturbance increases as θ is increased from 0° to 90°). In both disturbances the directivity observed was not expected to be exactly the one described by a pure dipole, because of various nonlinearities (i. e. supersonic pocket) and source noncompactness. However, a main dipole-like behavior, as the one detected in the oscillating flap case [15], was expected. The reason that the directivity is different for an oscillating flap and BVI seems to be related to the difference in phase between the two disturbances. Disturbance II has a higher frequency than disturbance I and also a different phase with respect to disturbance I. Thus, it may add or subtract differently in different directions for various cases. In the oscillating flap case the frequency and the phase difference are better forced than they are in the BVI case.

Now we will compare the noise signals resulting from types A, B and C shock motion (figs 16, 17 and 18, respectively). The two disturbances keep approaching each other as angle θ is increased because of the different disturbance origin. Angles $\theta = 70^o$ and 60°, seem to give the maximum

12

signal, if we measure from peak to peak, for types A and B respectively. (If we only look at the maximum absolute value then $\theta = 0^o$ seems to produce the greatest noise). For the case of type C we can see that the whole region between $\theta = 60^o$ and $\theta = 90^o$ produces about the same noise. For subsonic cases (not shown) the maximum noise is 90°, as it was mentioned above.

Figure 19 shows the directivity of the BVI for a NACA 0006 airfoil. In this case the two disturbances are closer to each other than the previous NACA 64A006 cases. If we increase θ, the two disturbances now fall on top of each other more quickly ($\theta = 90^o$). The noise becomes maximum at $\theta=90^o$, but still the noise at $\theta=60^o$ and 70° is not much lower. Similar observations can be made for all the other 4-digit airfoils tried (e. g. 1306, 1406, (0.5)406).

From the preceding discussion of BVI noise directivity we can conclude that the maximum noise occurs at around $\theta = 60^o$ - 90° ($\theta_v = 10^o$ - 30°), and depends on both disturbances I and II, but also on the phase difference between the two disturbances, that can be different for various airfoil shapes.

In order to isolate the effect of disturbance II in the maximum noise we compared (figure 20) the $Cp(T)$ signal at the same point ($\theta = 90^o$ and $r_v = 50$ chords) for NACA airfoils 0006, (0.5)406 and 1406 for the conditions specified before for figure 13 (i. e. same lift). It can be noted that the two disturbances are almost merged at this point. We can also see that the NACA 1406 airfoil has a larger signal, which is consistent to the fact that the same airfoil has a larger disturbance II as shown in figure 13.

In figure 21 we compared the signal for NACA airfoils with different points of maximum camber: 1306 and 1406, for angles of attack that produce the same lift: $\alpha=0.055^o$ and 0°, respectively. We looked at the point of maximum noise: $\theta = 90^o$ and $r_v = 50$ chords. We can see that the 1406 airfoil has the larger signal, as expected since the same airfoil has a larger disturbance II as shown in figure 14.

We also ran the previous 4-digit airfoils at subsonic Mach numbers at conditions producing the same lift. They all produced the same BVI disturbance at all angles, as expected (no disturbance II was observed). In conclusion, symmetric airfoils and airfoils with a point of maximum camber farther upstream seem to give less BVI noise for transonic conditions producing the same lift.

13

Conclusions

An existing numerical finite difference code VTRAN2 was modified to analyze noise due to transonic BVI. The two-dimensional unsteady transonic small disturbance equation was solved numerically using ADI techniques with monotone switches including viscous effects due to shock-boundary interaction and the cloud-in-cell method for the simulation of the vortex. The Kirchhoff's method was used to extend the numerically calculated two-dimensional near-field aerodynamic results to the three-dimensional linear acoustic far-field.

The viscous effect (shock/boundary layer interaction) on BVI noise was studied and was found to have only a weak influence. The effect of the three types of unsteady shock motion (A, B and C) was also investigated. The unsteady pressure coefficients $C_p(t)$ showed the existence of two main disturbances. The first one (I) is believed to be associated with the fluctuating lift coefficient (C_l) and has a strong forward directivity while the second one (II) is believed to be associated with the fluctuating drag coefficient (C_d) caused by the movement of the supersonic pocket and has a strong downward directivity. The maximum radiation occurs at an angle θ between 60° and 90° below the horizontal for an airfoil-fixed coordinate system and depends on both disturbances I and II and the details of the airfoil shape. Symmetric airfoils, and airfoils with a point of maximum camber further upstream seem to give less BVI noise for conditions producing the same lift.

It is hoped that this work can contribute toward the better understanding of the mechanisms of noise due to transonic BVI. In the future, we will study the influence of the details of airfoil shape, especially near the leading edge. We will also include the effects of an oscillating airfoil at the same time with a BVI that can be useful in actual helicopter cases (feathering).

Acknowledgements

References

1. George, A. R., "Helicopter Noise: State-of- the-Art," *Journal Aircraft*, Vol. 15, No. 11, November 1978, pp. 707-715.

2. Schlinker, R. H., and Amiet, R. K., "Rotor-Vortex Interaction Noise," NASA CR-3744, Oct. 1983.

3. Schmitz, F. H., and Yu, Y. H., "Helicopter Impulsive Noise: Theoretical and Experimental Status," in *Recent Advances in Aeroacoustics*, A. Krothapalli and C. A. Smith, editors, Springer-Verlag, NY, 1986.

4. George, A. R., Smith C. A., Maisel, M. D., and Brieger, J. T., "Tilt Rotor Aircraft Aeroacoustics,"*Proceedings of the 45th Annual Forum of the American Helicopter Society,* Boston, MA., May 1989.

5. Poling, D. R., Dadone, L., Telionis, D. P., "Blade-Vortex Interaction," *AIAA Journal*, Vol. 27, No. 6, June 1989, pp. 694-699.

6. George, A. R., and Chang, S. B., "Noise Due to Transonic Blade-Vortex Interactions," *Proceedings of the 39th Annual National Forum of the American Helicopter Society*, Paper A-83-39-50-D000, 1983.

7. George, A. R., and Chang, S. B., "Flow Field and Acoustics of Two-dimensional Transonic Blade-Vortex Interactions," AIAA Paper 84-2309, AIAA 9th Aeroacoustics Conference, Williamsburg, VA, October 15-17, 1984.

8. Ballhaus, W. F., and Goorjian, P. M., "Implicit Finite-Difference Computations of Unsteady Transonic Flows about Airfoil," *AIAA Journal.*, Vol. 15, No. 12, Dec. 1977, pp. 1728-1735.

9. Rizzetta D. P., and Chin, W. C., "Effect of Frequency in Unsteady Transonic Flow," *AIAA Journal*, Vol. 17, No. 7, July 1979, pp. 779-781.

10. Guruswamy P., and Goorjian P. M., "Effects of Viscosity on Transonic Aerodynamic and Aeroelastic Characteristics of Oscillating Airfoils" *AIAA Journal*, Vol 21, No. 9, Sept. 1984, pp.700-707.

11. Goorjian, P. M., Meagher, M. E., and Van Buskirk, R. D., "Monotone Switches in Implicit Algorithms for Potential Equations Applied to Transonic Flows" *AIAA Journal*, Vol 23, No. 4, Apr. 1985, pp. 492-498.

12. Goorjian, P. M., and Van Buskirk, R. D., "Second-Order-Accurate Spatial Differencing for the Transonic Small-Disturbance Equation" *AIAA Journal*, Vol. 23, No. 11, Nov. 1985, pp. 1693-1699.

13. Lyrintzis, A. S., and George, A. R., "VTRAN2: Computation of Two-dimensional Blade-Vortex Interactions Using the Unsteady Small Disturbance Equation, (User's Manual)" Cornell University, Ithaca NY, March 1986.

14. Lyrintzis, A. S. "Transonic Blade-Vortex Interactions," Ph.D. Dissertation, Mechanical and Aerospace Engineering Department, Cornell University, Ithaca NY, Jan. 1988.

15. Lyrintzis, A. S., and Xue, Y., "Acoustics of Transonic Flow Around an Oscillating Flap," submitted in the *Journal of Fluids Engineering* for publication, June 1990.

16. McCroskey, W. J., and Goorjian, P. M., "Interactions of Airfoils with Gusts and Concentrated Vortices in Unsteady Transonic Flow," AIAA Paper 83-1691, AIAA 16th Fluid and Plasma Dynamics Conference, Danvers, MA, July 1983.

17. Srinivasan, G. R., McCroskey, W. J., and Kutler, P., "Numerical Simulation of the Interaction of a Vortex with Stationary Airfoil in Transonic Flow," AIAA Paper 84-0254, AIAA 22nd Aerospace Sciences Meeting, Reno, Nevada, Jan., 1984.

18. Sankar, N. L., and Tang, W., "Numerical Solution of Unsteady Viscous Flow Past Rotor Sections," AIAA Paper 85-129, Jan. 1985.

19. Srinivasan, G. R., McCroskey, W. J., and Baeder J. D., "Aerodynamics of two-dimensional Blade-Vortex Interaction," *AIAA Journal*, Vol. 24 No. 10, Oct. 1986, pp. 1569-1576.

20. Owen S. T., and Shenoy R. K., "Numerical Investigation of Two-Dimensional Blade-Vortex Interaction," *Proceedings of the AHS National Specialists' Meeting on Aerodynamics and Aeroacoustics*, Arlington, Texas, Feb. 25-27, 1987.

21. Damodaran, M., and Caughey, D. A., "A Finite Volume Euler Calculation of the Aerodynamics of Transonic Airfoil-Vortex Interaction," *AIAA Journal*, Vol. 26, No. 11, Nov. 1988, pp.1346-1353.

22. Baeder, J. D., McCroskey, W. J., and Srinivasan, G. R.,"Acoustic Propagation Using Computational Fluid Dynamics," *Proceedings of the 42nd Annual Forum of the American Helicopter Society*, Washington, DC, June, 1986, Vol. 1, pp. 551-562.

23. Baeder, J. D., "Computation of Non-Linear Acoustics in Two-Dimensional Blade-Vortex Interactions," 13th European Rotorcraft Forum, Arles, France, Sept. 1987.

24. Liu, N. S. Davoudzadeh, F., Briley, W. R., and Shamroth, S. J., "Navier Stokes Simulation of Transonic Blade-Vortex Interactions," *Proceedings of the International Symposium on Nonsteady Fluid Dynamics (ASME)*, Miller, J. A., and Telionis, D. P., editors, Toronto, Canada, June 1990, pp 177-186.

25. George, A. R., and Lyrintzis, A. S., "Acoustics of Transonic Blade-Vortex Interactions," *AIAA Journal*, Vol. 26, No. 7, July 1988, pp. 769-776.

26. Lyrintzis, A. S., and George, A. R., "Far-Field Noise of Transonic Blade-Vortex Interactions," *American Helicopter Society Journal*, Vol. 34, No.3, July 1989, pp.30-39.

27. Lyrintzis, A. S., and George, A. R., "The Use of Kirchhoff Method in Acoustics," *AIAA Journal*, Vol. 27, No. 10, Oct. 1989, pp. 1451-1453.

28. Lyrintzis, A. S., and George, A. R., "Study of Transonic Blade-Vortex Interaction Noise,"*Noise Control Engineering Journal*, Vol. 32. No. 3, May-June 1989, pp.105-109.

29. Lyrintzis, A. S. "Transonic Blade-Vortex Interactions: a Parametric Study" NACA CR in preparation.

30. Ballhaus, W. F., "Some Recent Progress in Transonic Flow Computations," in *Numerical Methods in Fluid Dynamics*, ed. Wirz H. J., and Smolderen J. J., McGraw Hill, NY 1978, pp. 155-235.

31. Rizzetta, D. P., "Procedures for the Computation of Unsteady Transonic Flow Including Viscous Effects," NASA CR-166249, 1982.

32. Poling, D. R., Telionis, D. P., "The Response of Airfoils to Periodic Disturbances-The Unsteady Kutta Condition," *AIAA Journal*, Vol.24, No.2, Feb. 1986, pp. 193-199.

33. Chang, S. B., "Aerodynamics and Acoustics of Transonic Two-Dimensional Blade-Vortex Interactions," Ph.D. Dissertation, Mechanical and Aerospace Engineering Department, Cornell University, Ithaca NY, Jan. 1985.

34. Morgans, R. P. "The Kirchhoff Formula Extended to a Moving Surface," Philosophical Magazine, 9 (s.7, No. 55), 1930, pp. 141-161.

35. Morino, L., "A General Theory of Unsteady Compressible Potential Aerodynamics," NASA Contractor Report CR-2464, December 1974.

36. Morino, L., "Steady, Oscillatory, and Unsteady Subsonic and Supersonic Aerodynamics - Production Version 1.1 (SOUSSA-P, 1.1), Vol. 1, Theoretical Manual," NASA Contractor Report CR-159130, 1980.

37. Farassat, F., and Myers M. K., "Extension of Kirchhoff's formula to Radiation from Moving Surfaces," *Journal of Sound and Vibration*, Vol. 123, No. 3, 1988, pp.451-460.

38. Tijdeman, H., "Investigations of the Transonic Flow Around Oscillating Airfoils," NLR TR 77090- U, NLR The Netherlands, 1977.

39. Tangler, J. L., "Schlieren and Noise Studies of Rotors in Forward Flight," Paper 77, 33-05, Presented at the 33rd Annual National Forum of the American Helicopter Society, Washington, D. C., May 1977.

40. Caradonna, F. X., Laub, G. H., and Tung, C., "An Experimental investigation of the Parallel Blade-Vortex Interaction," 10th European Rotorcraft Forum, The Hague, Netherlands, August 1984.

41. Shenoy, R. K. "Aeroacoustic Flowfield and Acoustics of a Model Helicopter Tail Rotor at a High Advance Ratio," *Proceedings of the 45th Annual Forum of the American Helicopter Society*, Boston, MA., May 1989.

42. Martin, M. R., and Splettstoesser, W. R., "Acoustic Results of the Blade-Vortex Interaction Acoustic Test of a 40 Percent Model Rotor in the DMW," *Proceedings of the American Helicopter Society National Specialists' Meeting on Aerodynamics and Aeroacoustics*, Arlington, Texas, Feb. 1987.

17
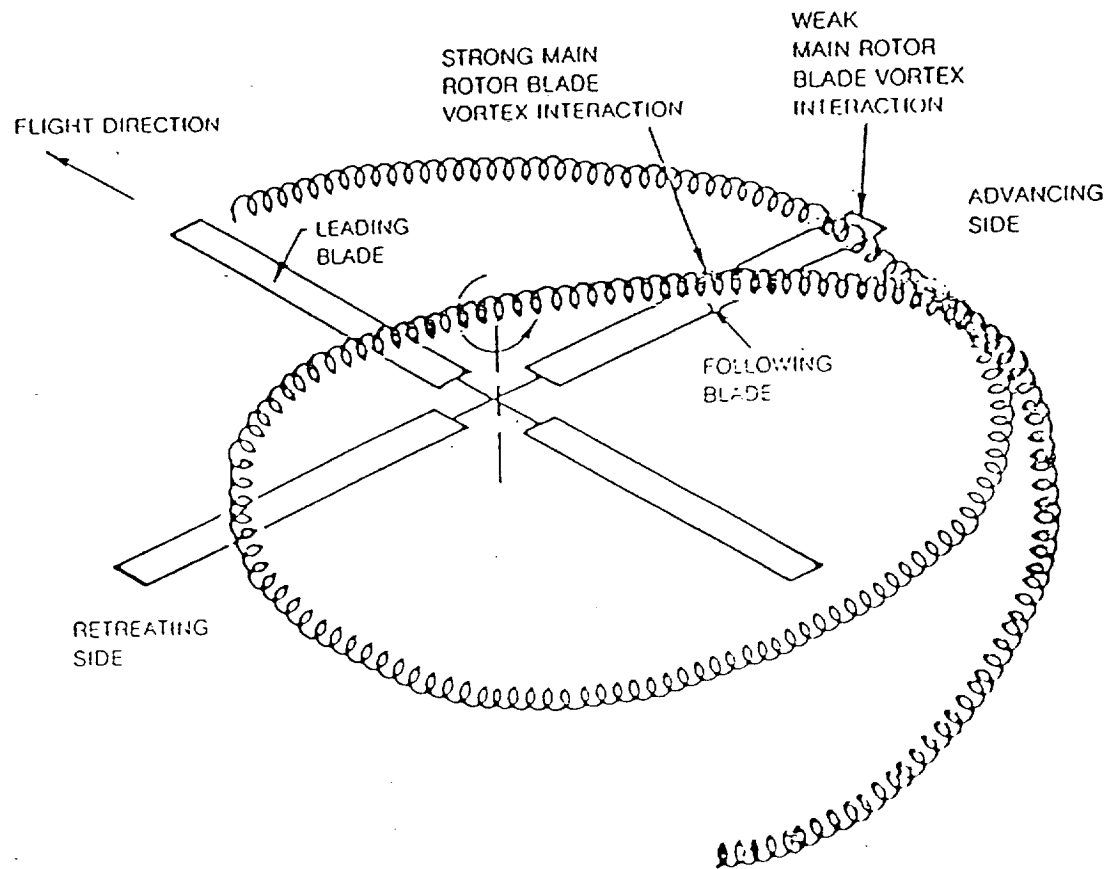
Figure 1. Formulation of BVI for a four bladed rotor (from Schlinker and Amiet [2]).

VORTEX PARALLEL TO BLADE
(TWO-DIMENSIONAL CASE)

Γ

(x_v, y_v)

TWO-DIMENSIONAL CASE:
SIDE VIEW
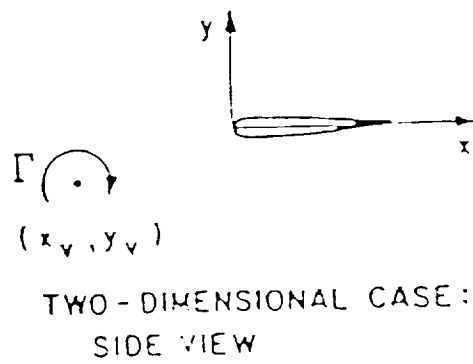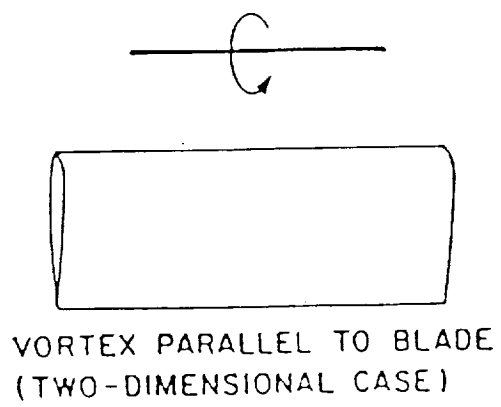
Figure 2. Two-dimensional BVI.
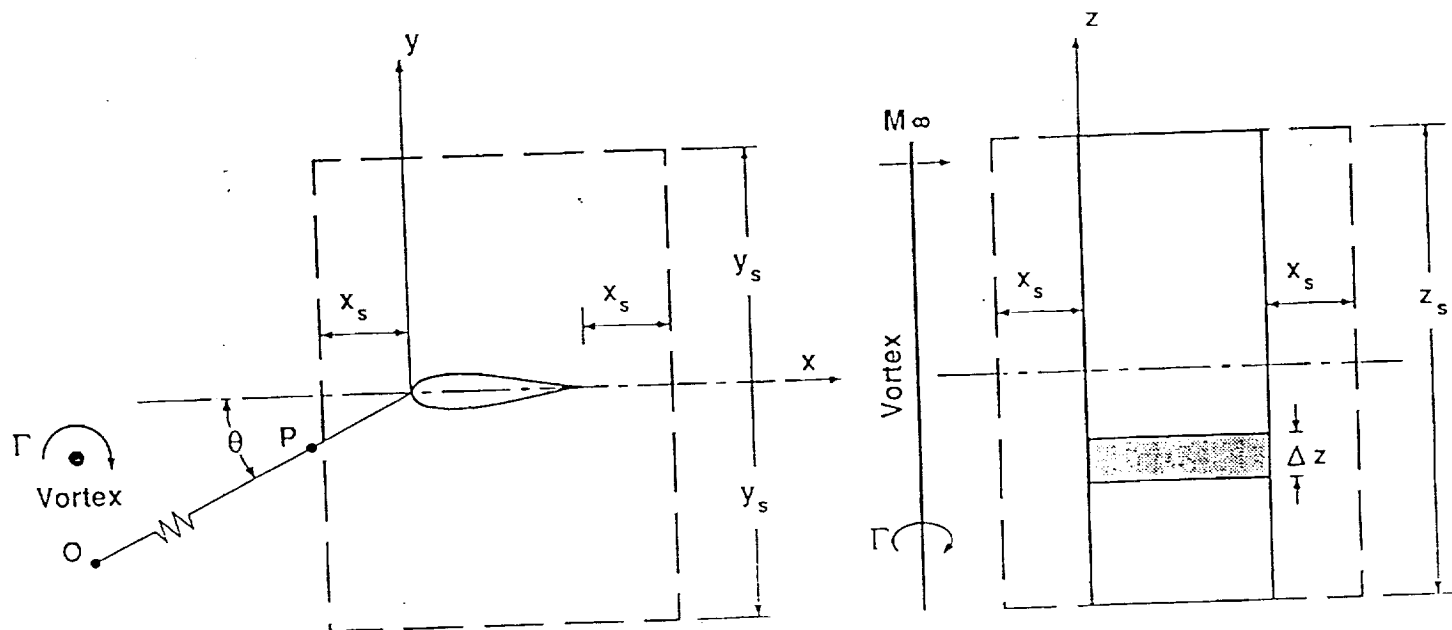
Figure 3. Kirchhoff's surface for the calculation of the far-field.

Type A
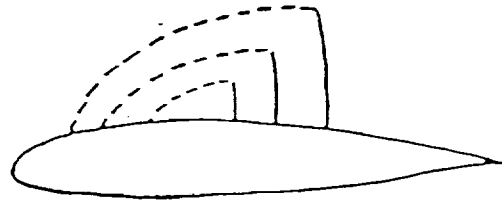
Type B
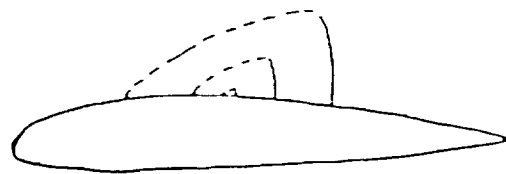
Type C
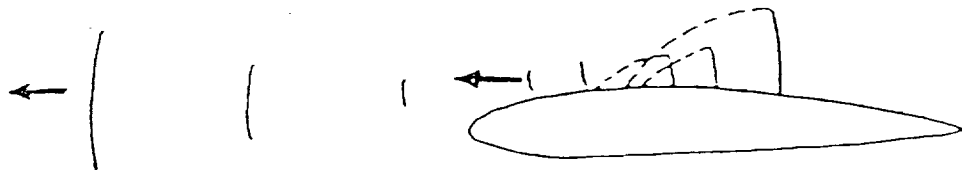
Figure 4. Tijdeman's unsteady types of shock motion.
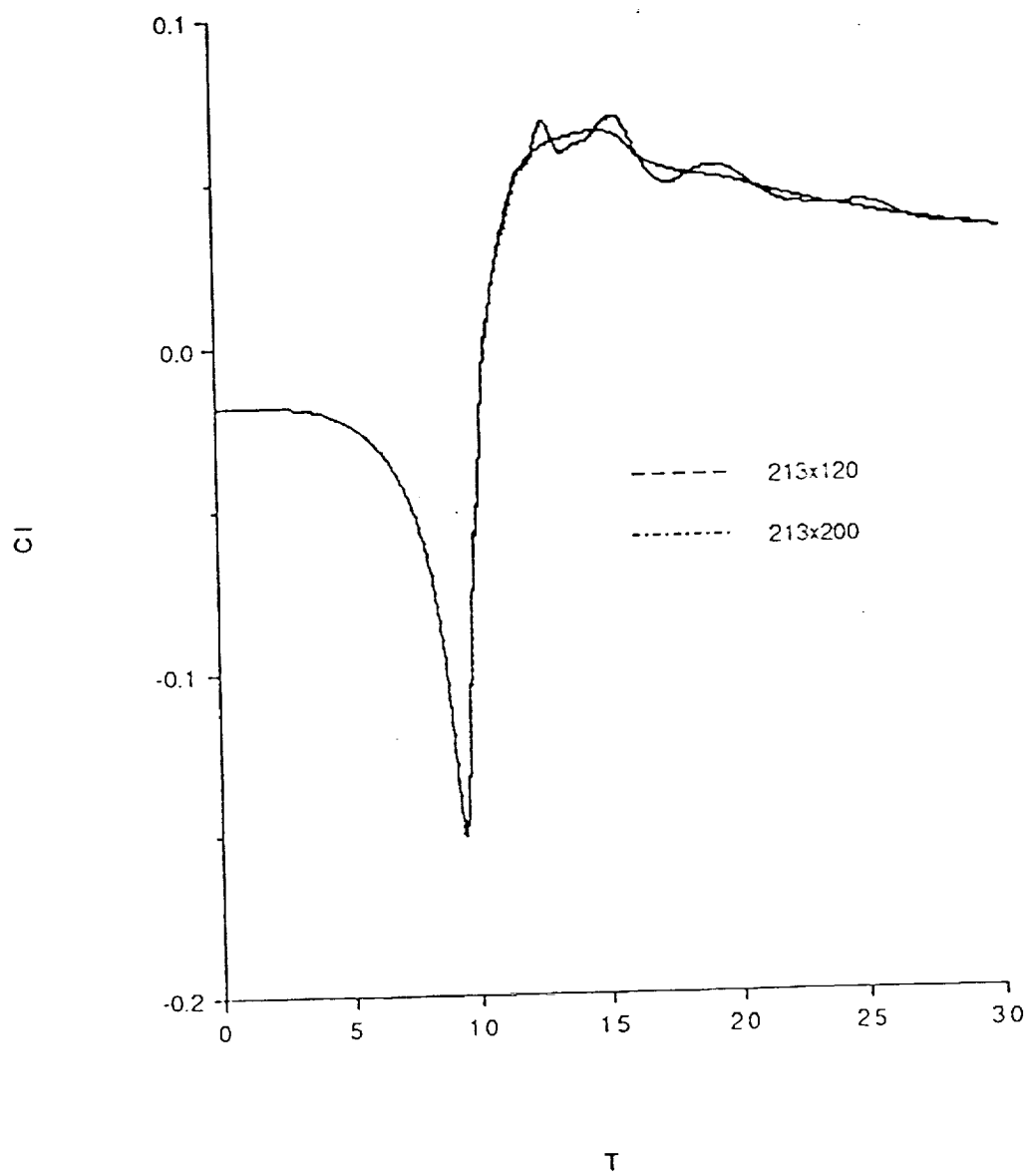
Figure 5. Effect of y-grid size on the $C_1(T)$ signal for type C.
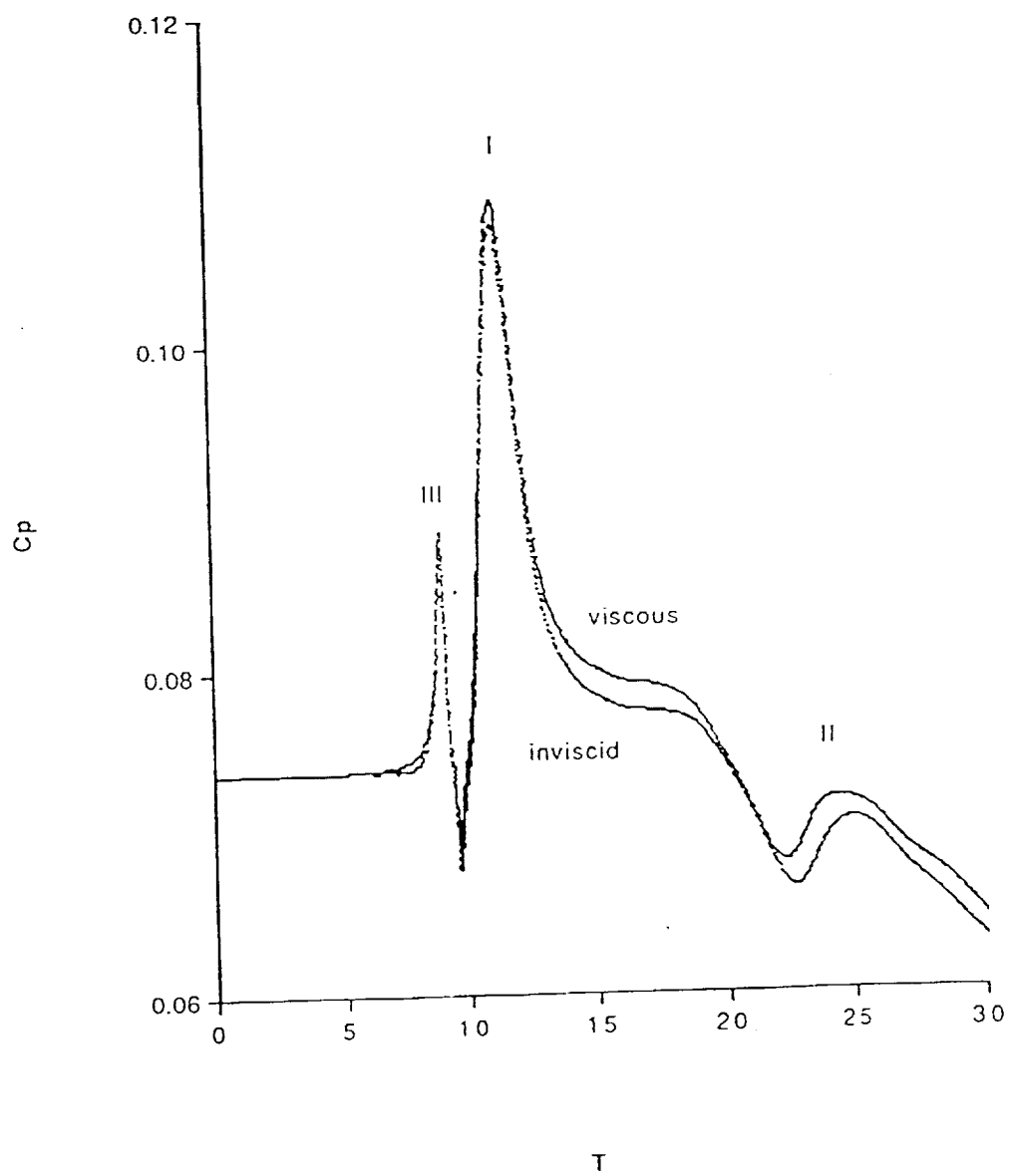
Figure 6. Effect of viscosity on the $C_p(T)$ signal for type A; point P (x=-0.3000, y=-0.17478).
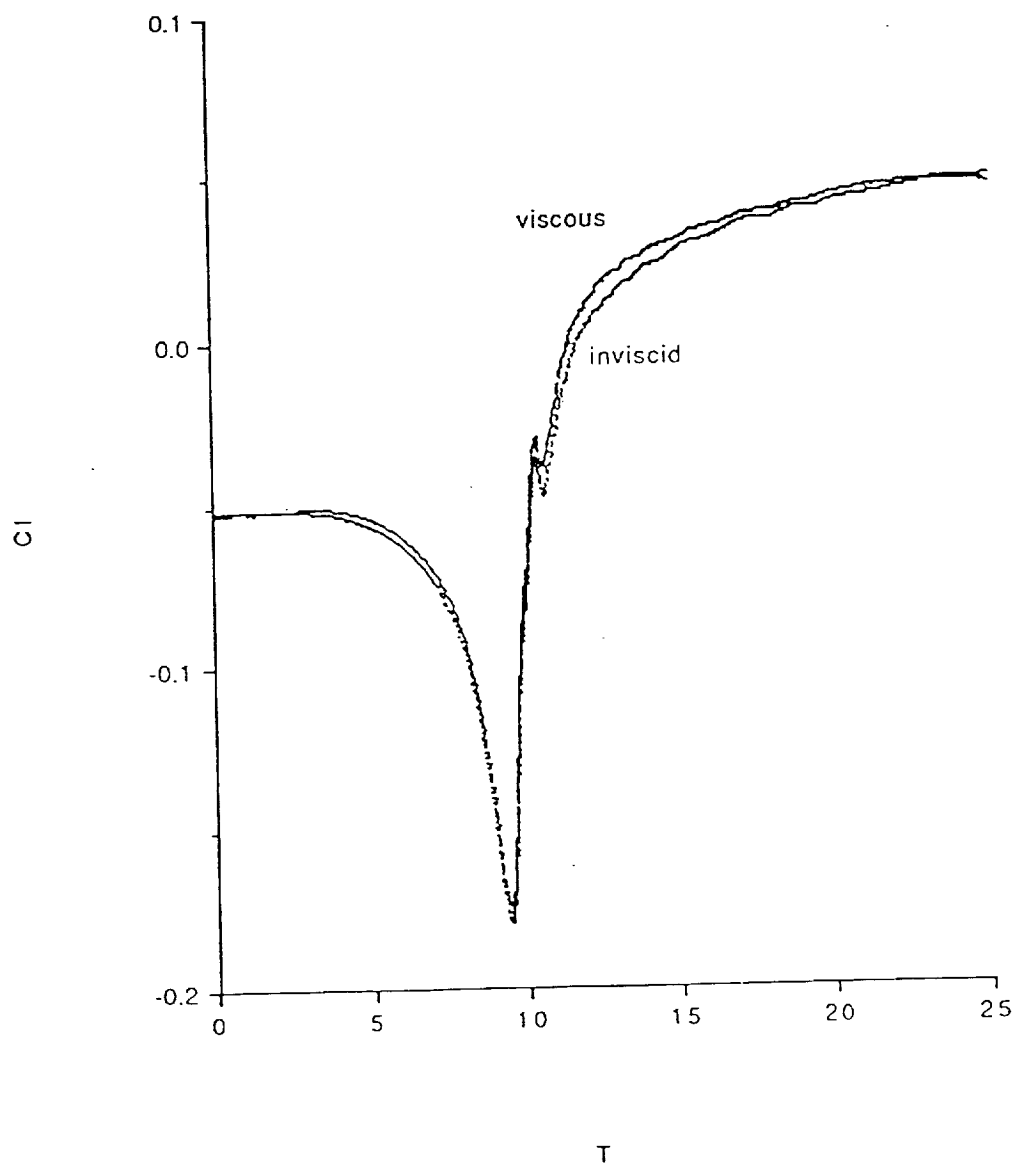
Figure 7. Effect of viscosity on the $C_l(T)$ signal for type A.
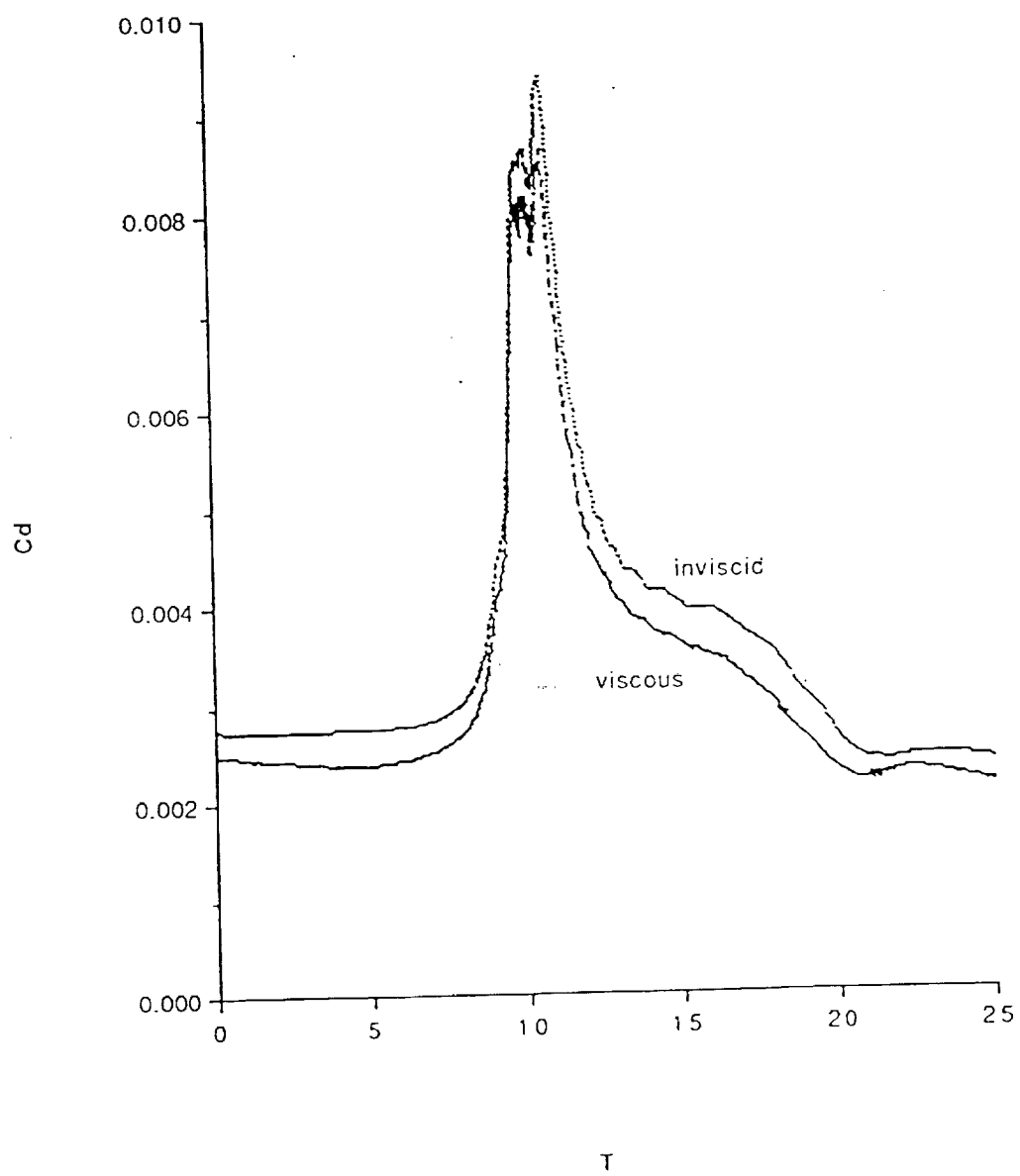
Figure 8. Effect of viscosity on the $C_d(T)$ signal for type A.
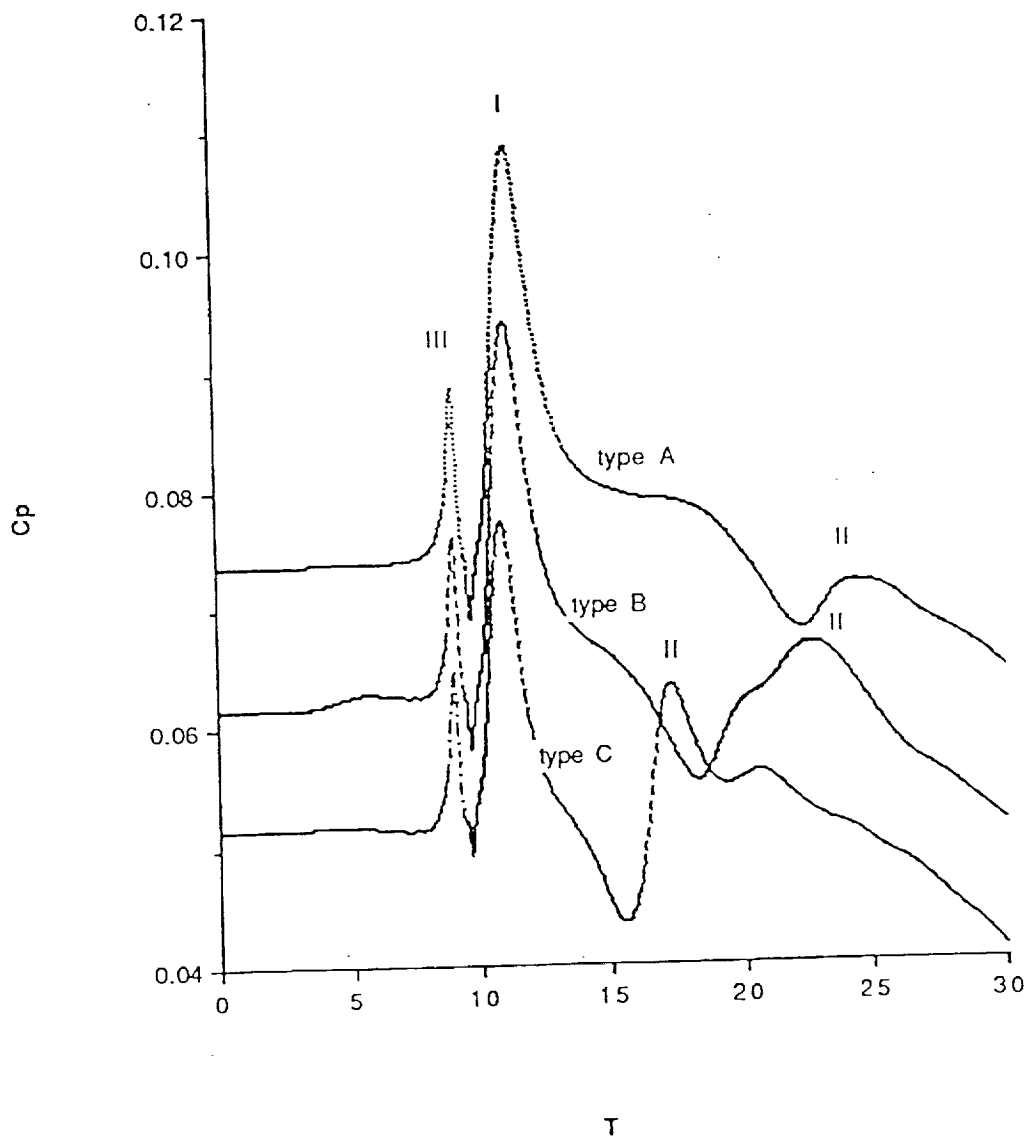
Figure 9.   Comparison of the near-field BVI noise for types A, B, C;
point P (x=-0.3000, y=-0.17478).
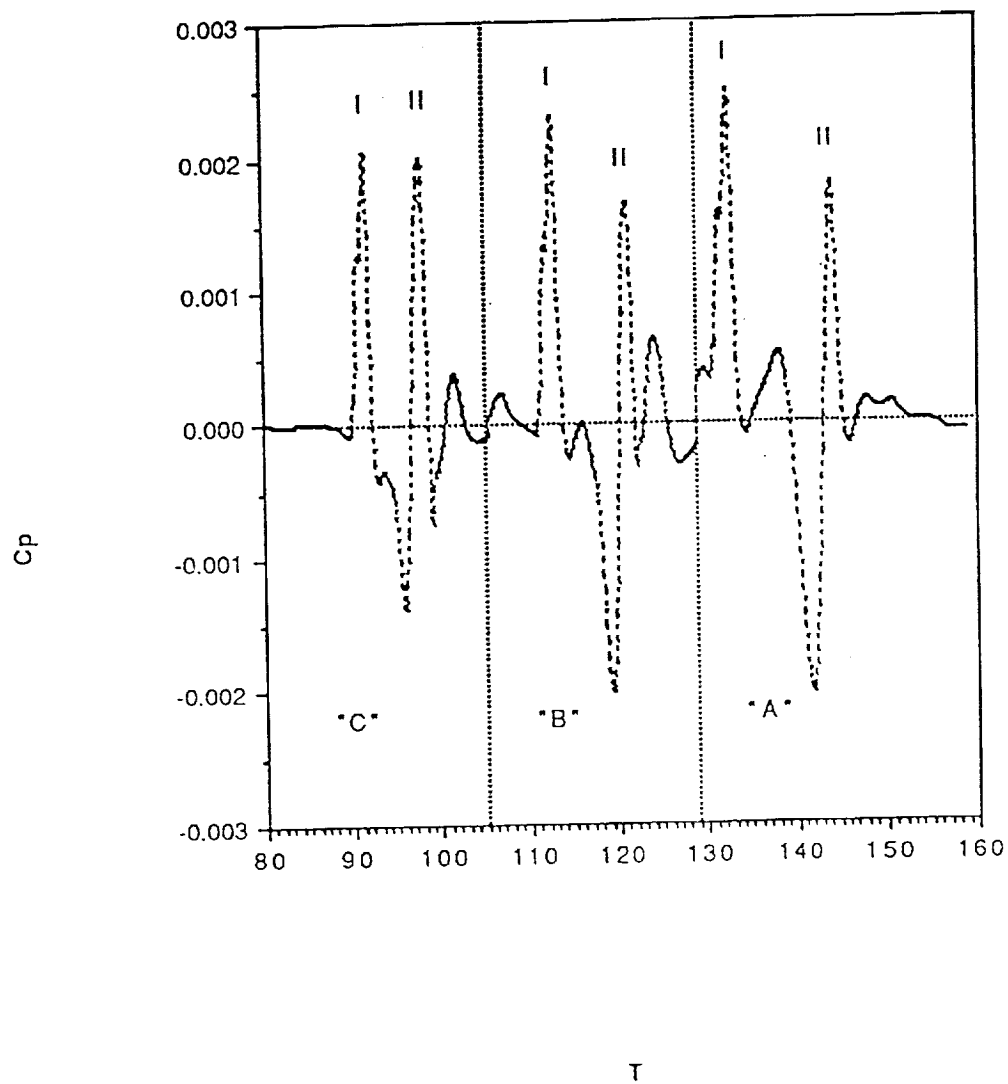
Figure 10.   Comparison of the far-field BVI noise for types A, B, C;
point O (r = 20 chords, θ = 30°, span = 8 chords)

Figure 11. Comparison of the C_l (T) signal for BVI, types A, B, C.
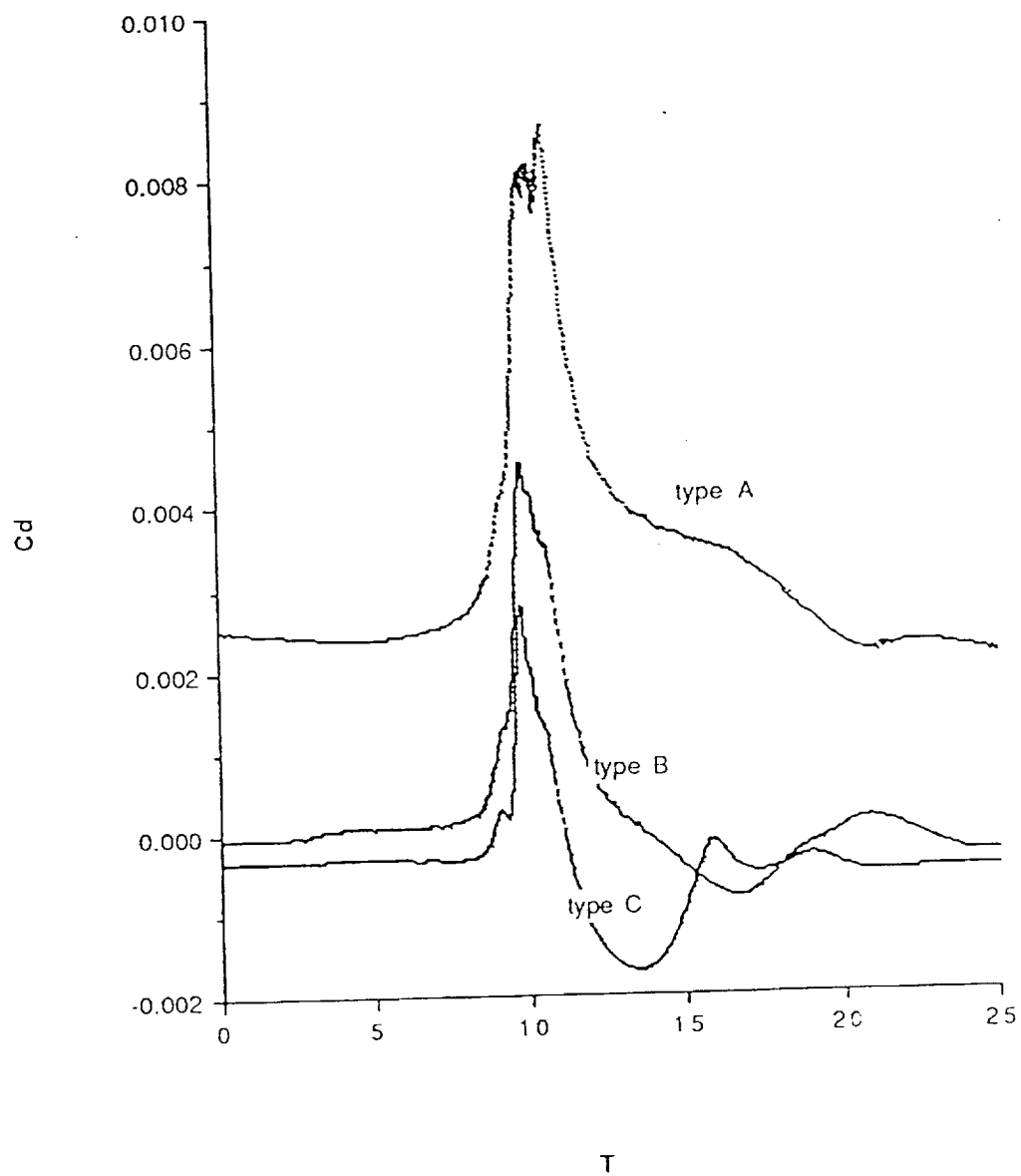
Figure 12. Comparison of the C_d (T) signal BVI for types A, B, C.
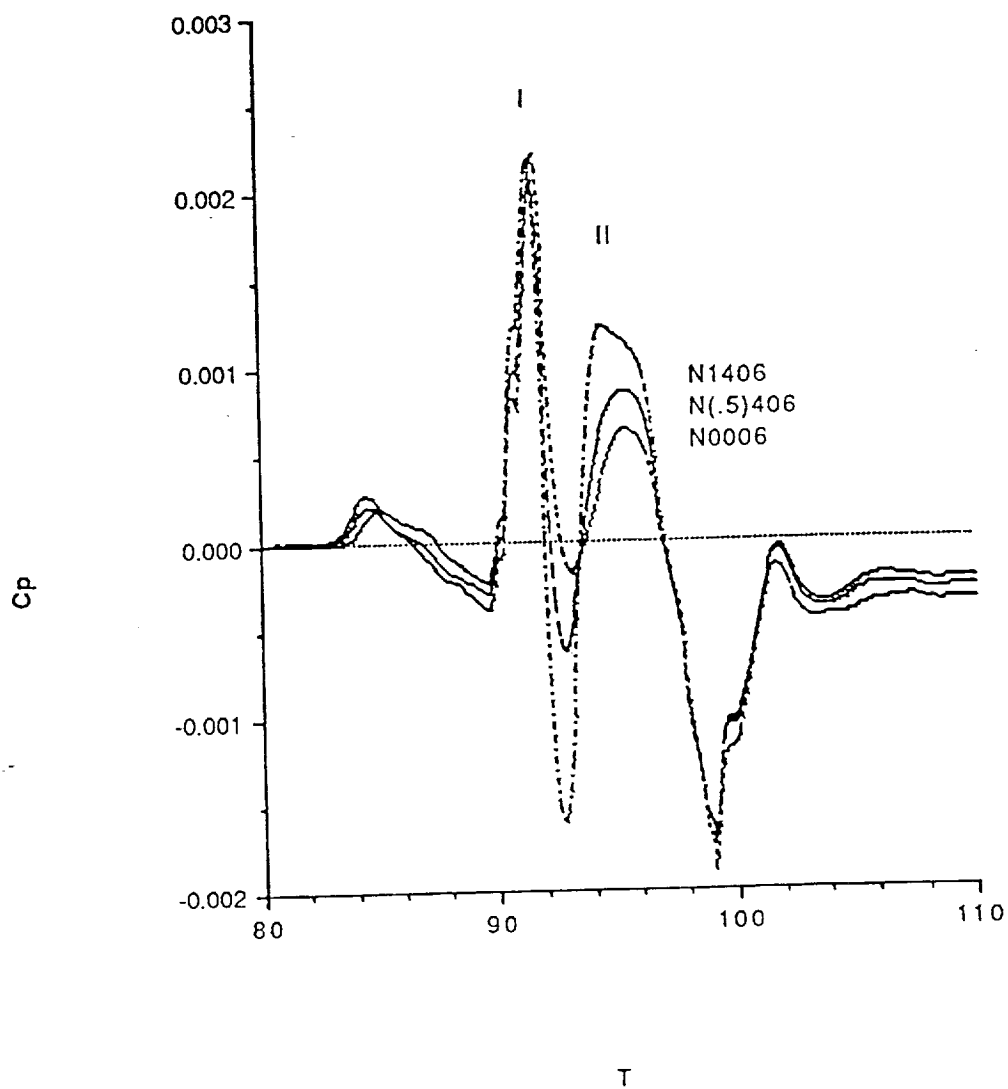
Figure 13.   Comparison of the far-field noise for NACA 0006 (α=1.051°), (0.5)406 (α=0.536°) and 1406 (α=0°), initial C_l = 0.229 in all cases; point O (r = 20 chords, θ=30°, span = 8 chords).

Figure 14. Comparison of the far-field noise for NACA 1306 ($\alpha=0.055°$) and 1406 ($\alpha=0°$), initial $C_1 = 0.229$ in both cases; point O ($r = 20$ chords, $\theta=30°$, span = 8 chords).
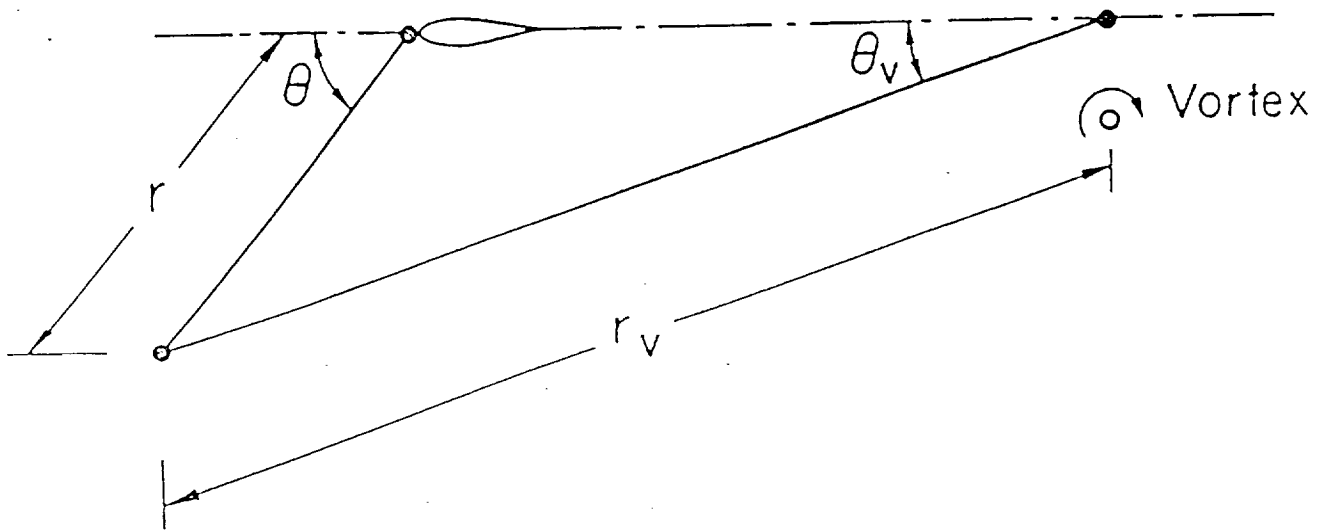
Figure 15. Relation between an airfoil fixed and a vortex fixed coordinate system.
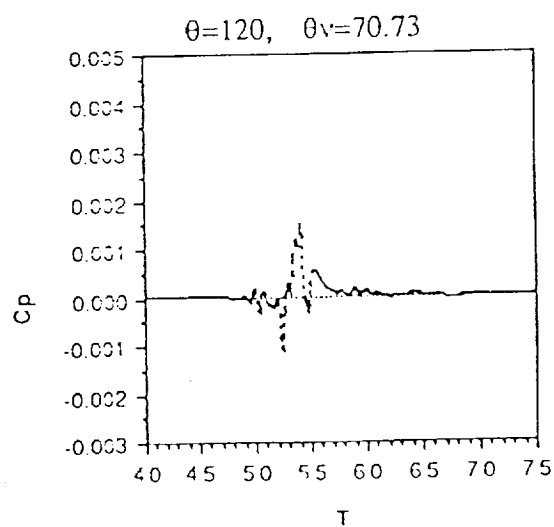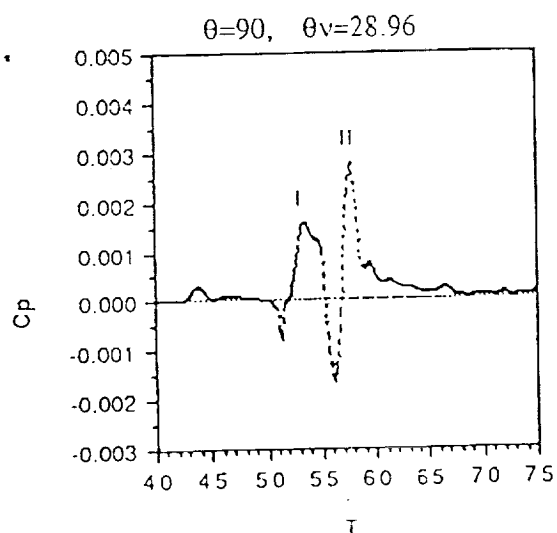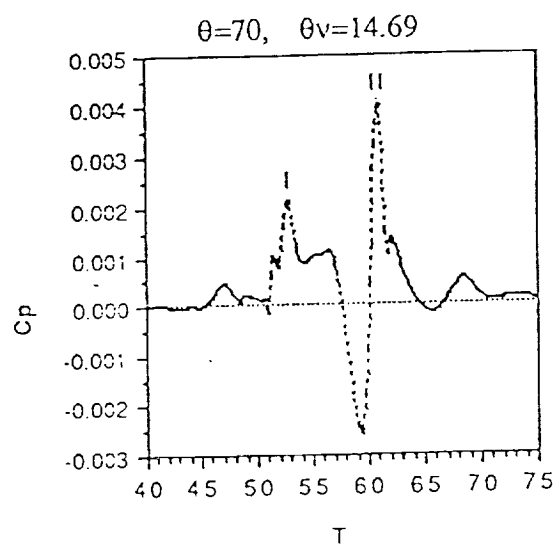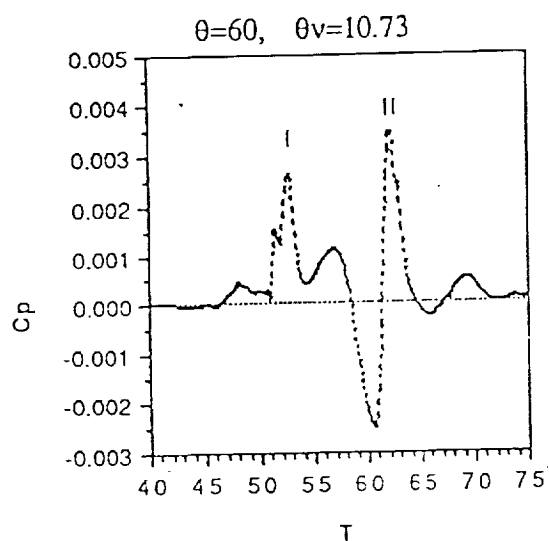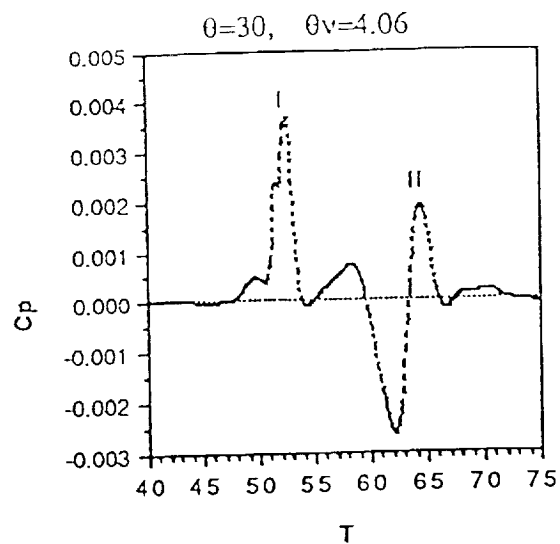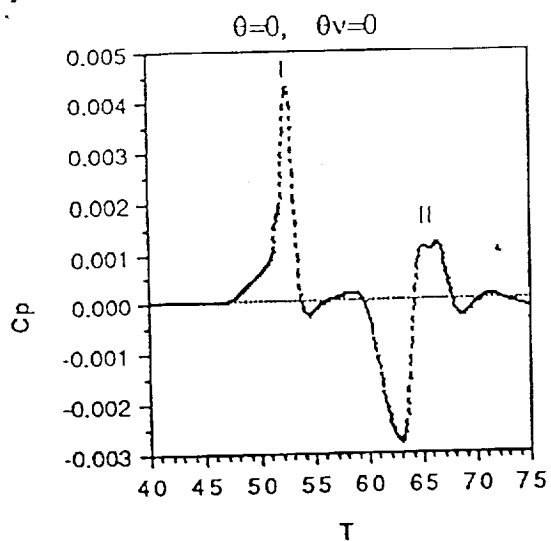
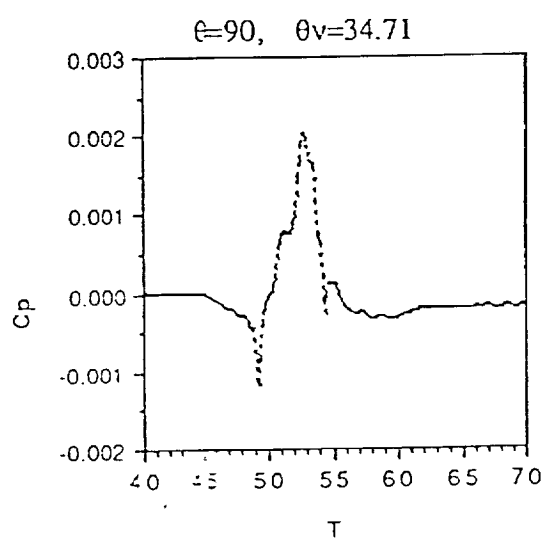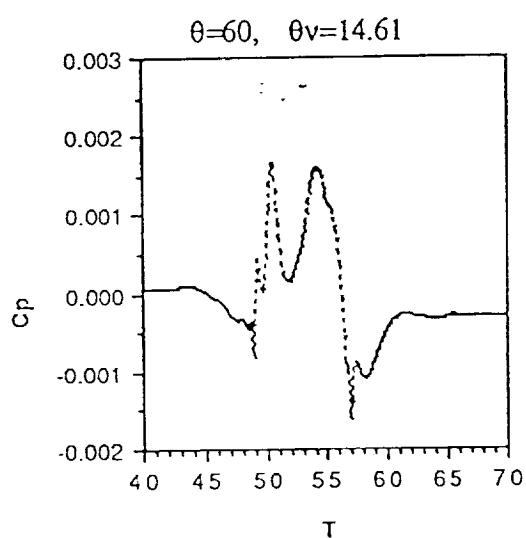Figure 16. BVI noise directivity for type A; $r_V = 50$ chords, span = 4 chords.
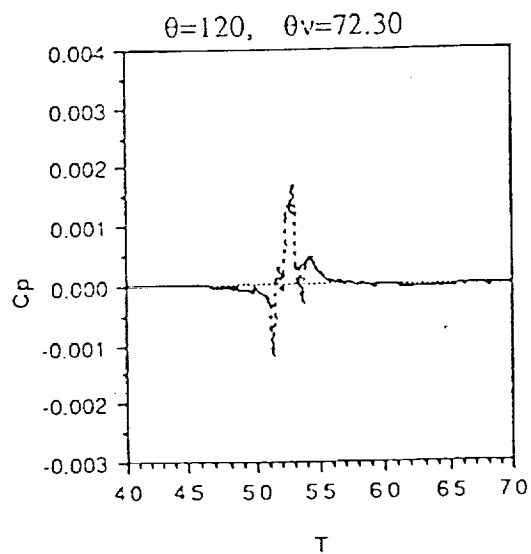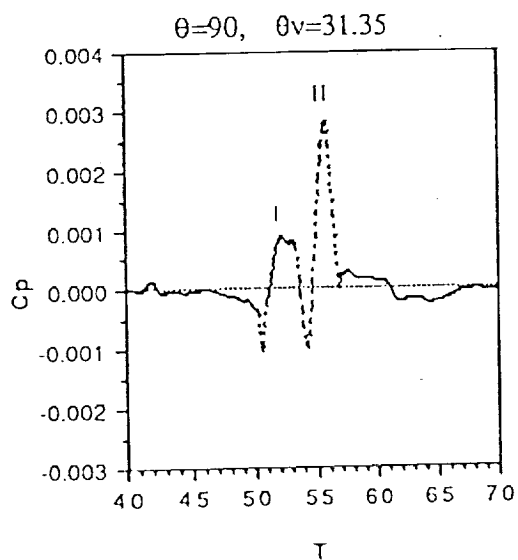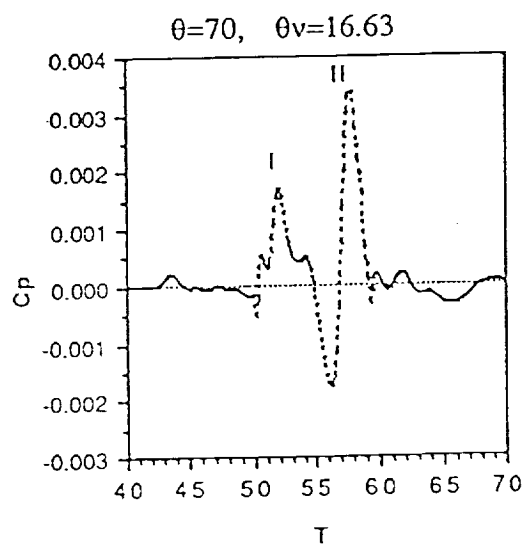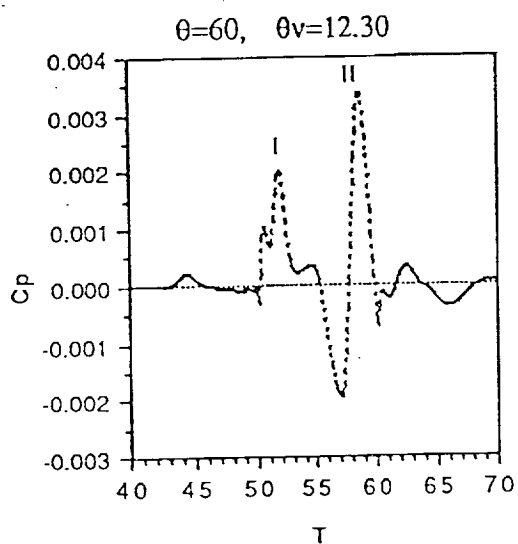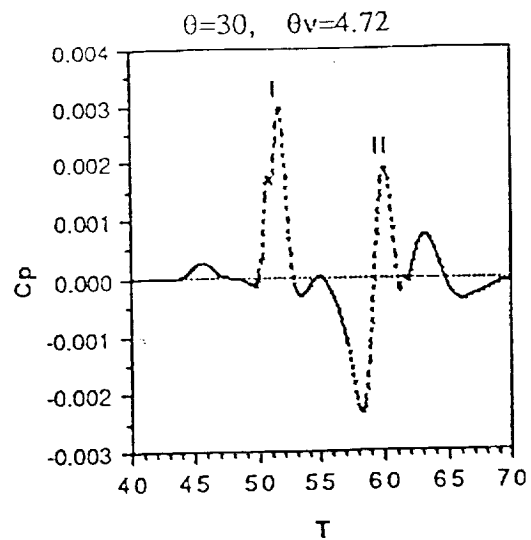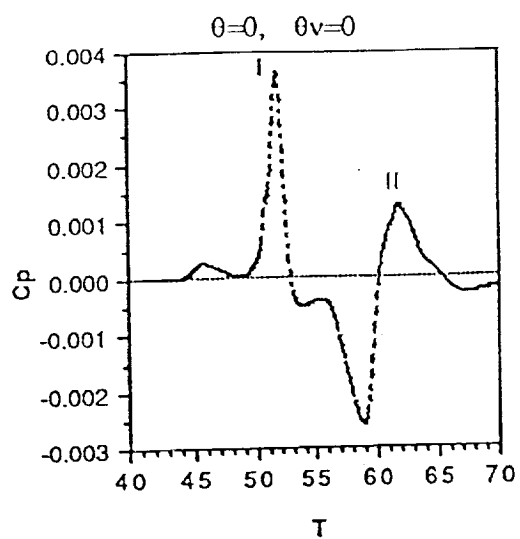
Figure 17. BVI noise directivity for type B; $r_v = 50$ chords, span $= 4$ chords.
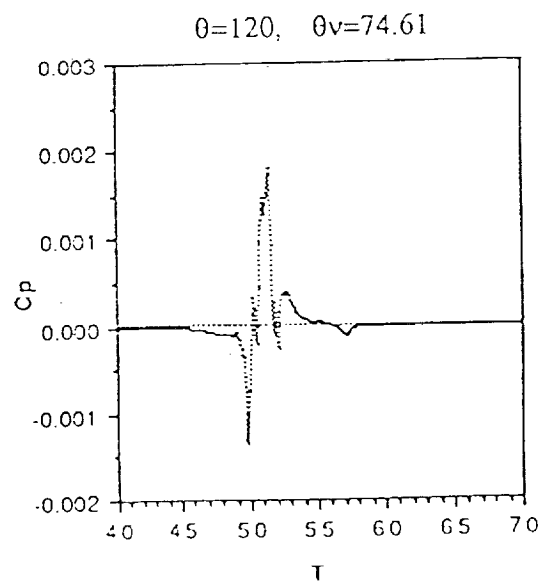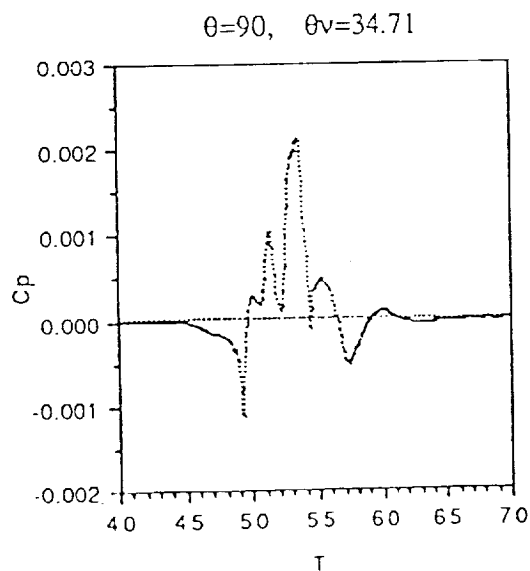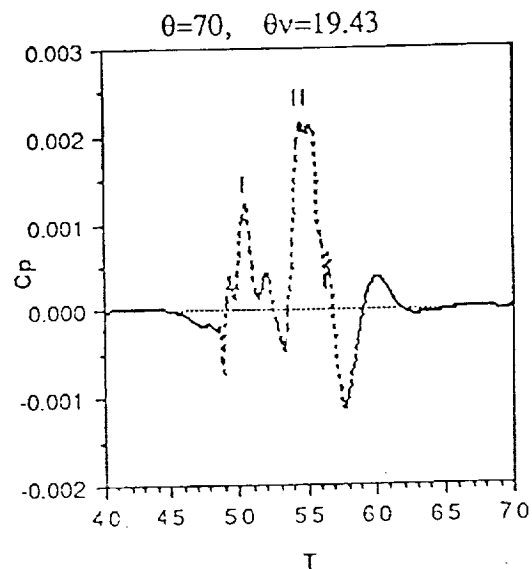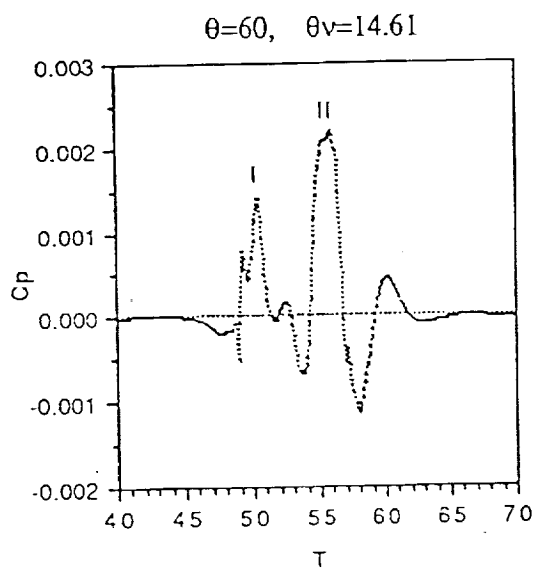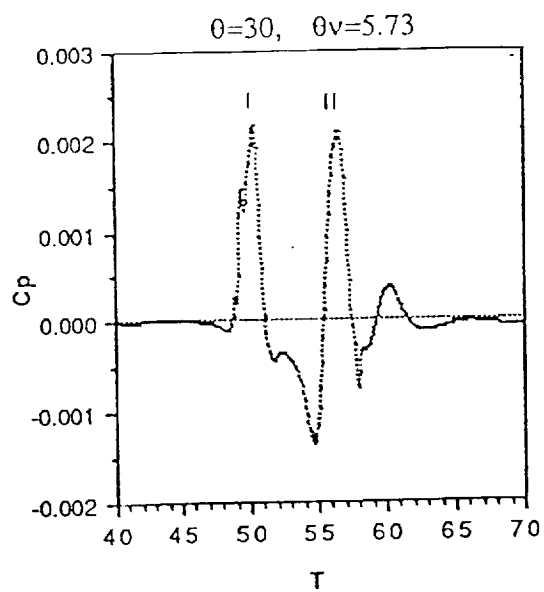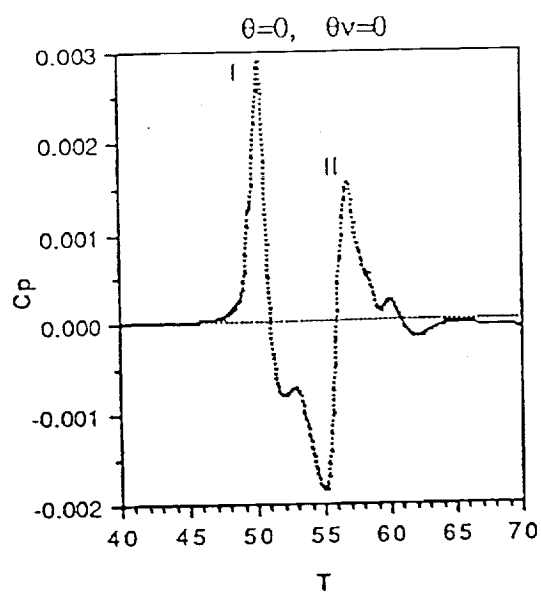
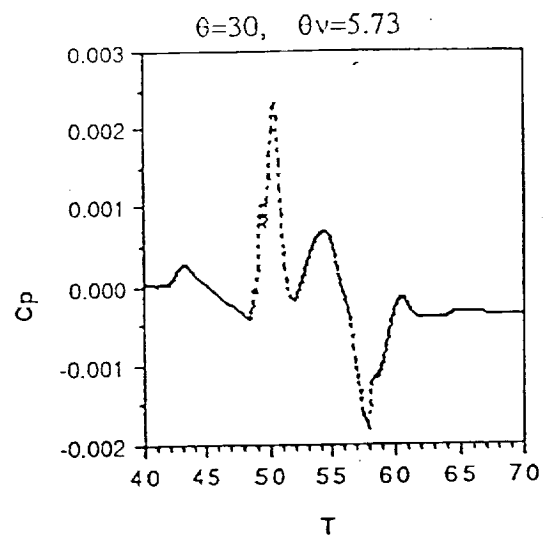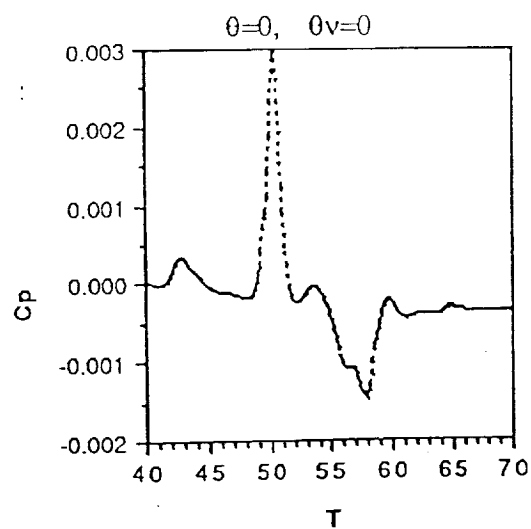Figure 18. BVI noise directivity for type C; $r_v = 50$ chords, span = 4 chords.
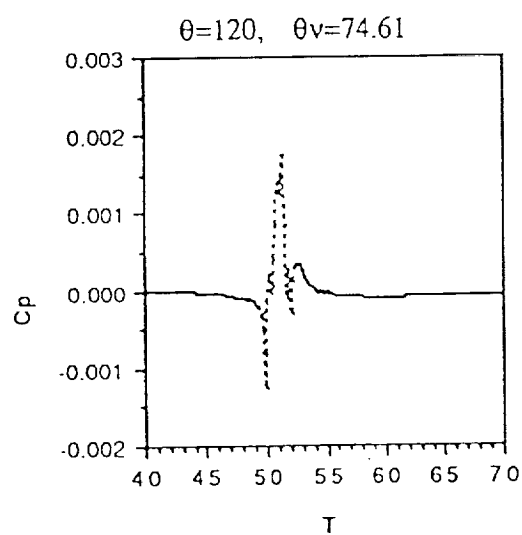
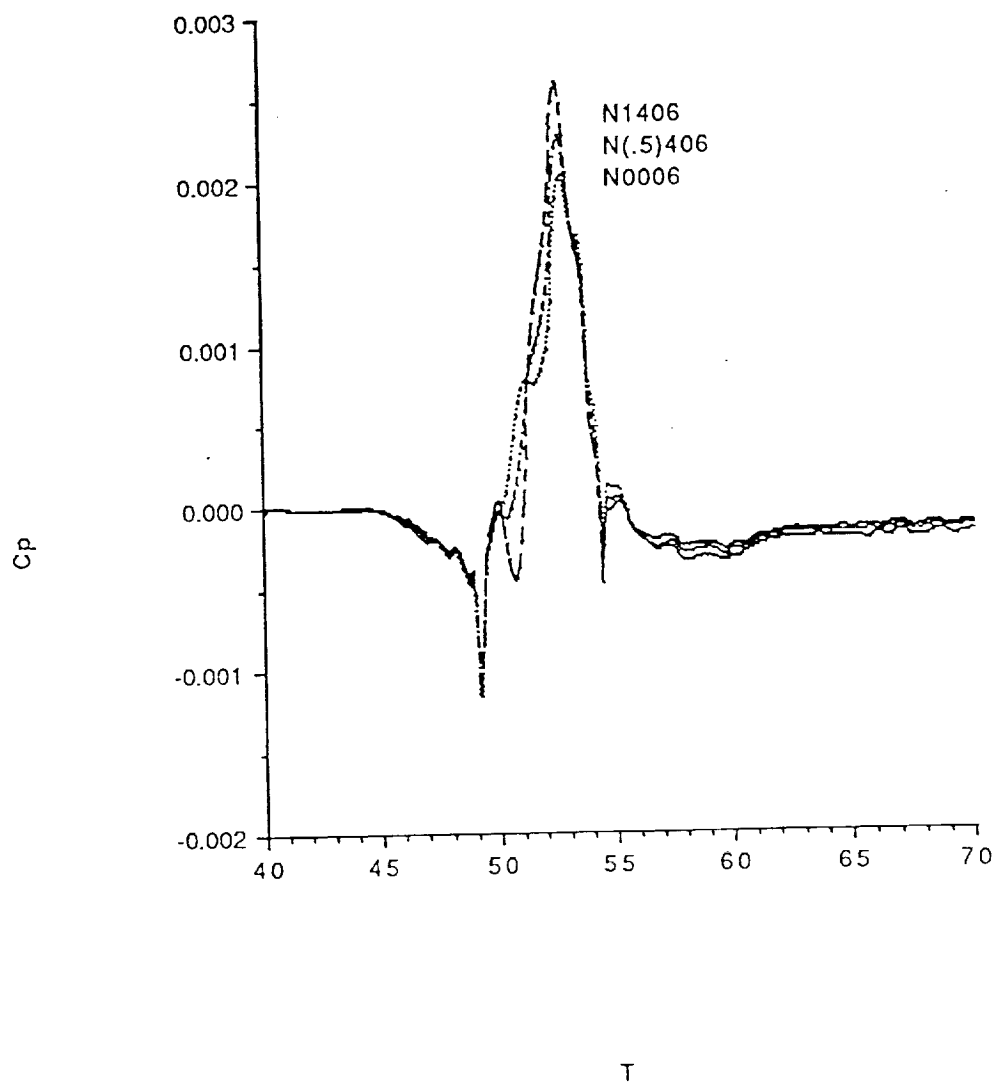Figure 19. BVI noise directivity for NACA 0006; $r_v = 50$ chords, span = 4 chords.

Figure 20. Comparison of the far-field noise for NACA 0006 ($\alpha=1.051^{\circ}$), (0.5)406 ($\alpha=0.536^{\circ}$) and N1406 ($\alpha=0^{\circ}$), initial $C_l = 0.229$ in all cases; $\theta = 90^{\circ}$, $r_v = 50$ chords, span = 4 chords.
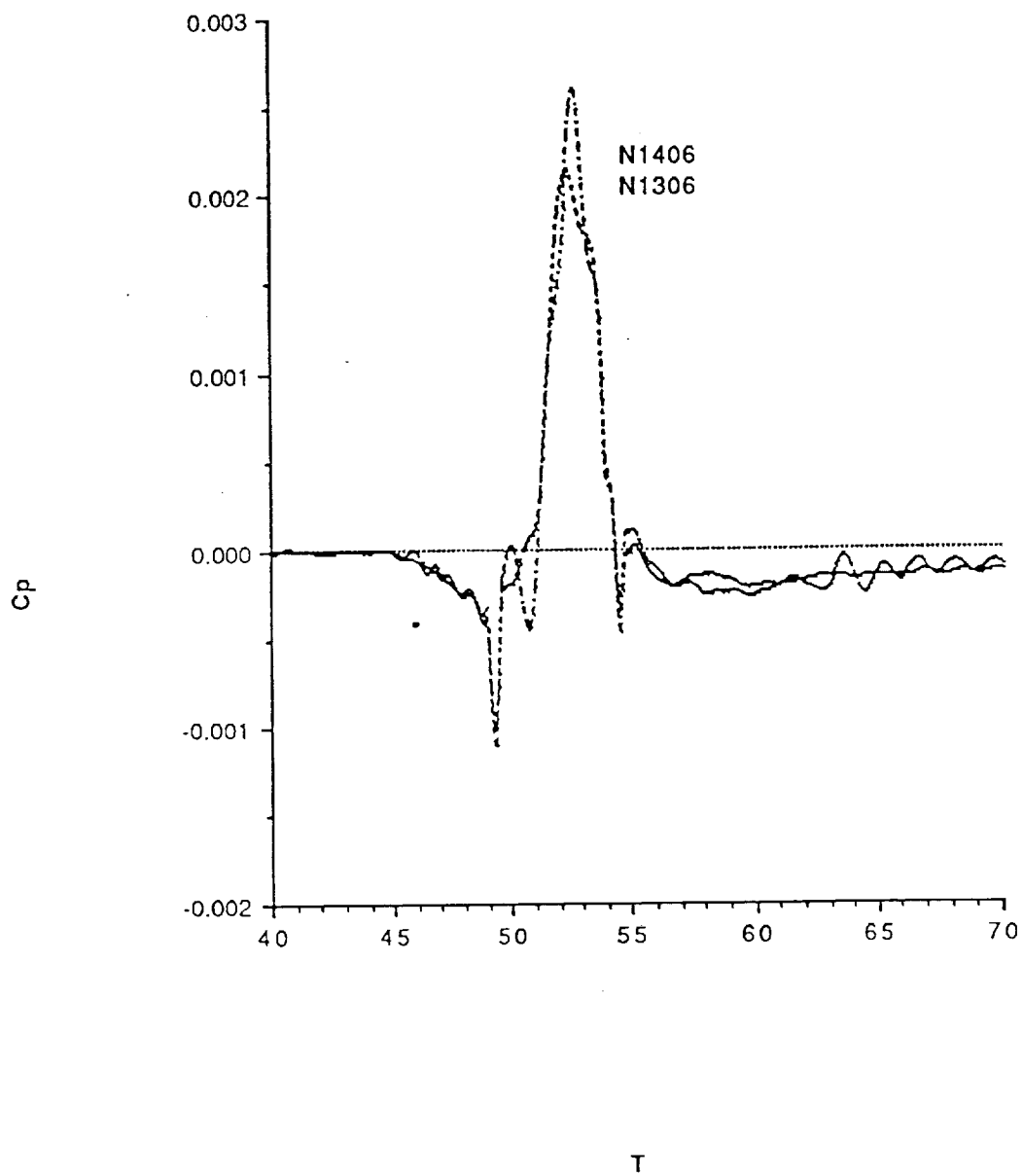
Figure 21. Comparison of the far-field noise for NACA 1306 ($\alpha=0.055^{\circ}$) and 1406 ($\alpha=0^{\circ}$), initial C_l = 0.229 in both cases; $\theta = 90^{\circ}$, r_v = 50 chords, span = 4 chords.